All–Optical Guided Wave Switching

Costantino De Angelis, Daniele Modotto, Andrea Locatelli and Stefan Wabnitz

Abstract Optical switching is a key functionality for enabling transparent all-optical networks. We present an overview of optical switching devices, based on either optical or electrical control signals, which permit to avoid the necessity of optics-electronics-optics conversion. We describe the basic principles of various guided wave optical switching devices, which exploit either relatively long interaction lengths in order to reduce the operating power requirements, or strong transverse confinement to reduce device dimensions. These devices include nonlinear mode couplers and interferometers based on optical fibers, as well as integrated waveguides based on photonic crystal structures or surface wave interactions in novel materials such as graphene.

1 Introduction: All–Optical Switching using Guided–Waves

In recent years, telecommunication networks have witnessed a dramatic increase of capacity, mostly driven by the exponential growth of IP traffic. Researchers had to tackle and solve several problems, and certainly the challenge of realizing transparent all optical switching was among the most important issues which have been addressed. In this framework, the goal is to use optics not only at the transmission level, but also at the switching level; this in turn requires to conceive devices which can perform switching directly in the optical domain, thus overtaking the unavoidable limitations of switching at the electronic level. Remarkably the goal can be achieved using either an optical or an electrical control; the common denominator is not the physical nature of the control signal, but the possibility of avoiding optics-electronics-optics (OEO) conversions which lead to inefficient and nontransparent switching.

Costantino De Angelis, Daniele Modotto, Andrea Locatelli, and Stefan Wabnitz
Dipartimento di Ingegneria dell'Informazione, Università di Brescia, Via Branze 38, Brescia 25123, Italy. e-mail: stefano.wabnitz@ing.unibs.it

In particular, in this paper we review some basic ideas and devices for all-optical switching in guided wave geometries, as this scenario offers important possibilities for tuning the light confinement, and thus exploring more efficient light–matter interactions. In section 2 we will discuss some relevant examples of all–optical switching devices exploiting optical fibers; in section 3 we will move into the field of integrated optics and we will discuss optical switching in photonic crystal waveguides, as well as using surface waves as a tool to enhance light matter–interactions in novel nonlinear materials such as graphene.

2 All Optical Pulse Switching in Optical Fibers

We review the different implementations of switching in optical fibers, including polarization effects in both high and low-birefringence fibers, and nonlinear optical loop mirrors. Both self-switching and two-beam, phase or cross-phase modulation (XPM) controlled switching will be analyzed.

2.1 Nonlinear Mode Coupling

We start by considering the continuous wave (CW) case and focus our attention on the linear and nonlinear coupling between the two modes of a structure composed of two waveguides placed in close proximity. The basic model to describe the evolution of the modal amplitudes $A_{1,2}$ along the coupler [1] is given by the following coupled equations:

$$
\begin{aligned}
& i\frac{dA_1}{dz} + CA_2 + \gamma\left[|A_1|^2 + \rho|A_2|^2\right]A_1 = 0 \\
& i\frac{dA_2}{dz} + CA_1 + \gamma\left[|A_2|^2 + \rho|A_1|^2\right]A_2 = 0
\end{aligned}
\tag{1}
$$

where C is the linear coupling coefficient, γ is the nonlinear coefficient and ρ is the XPM factor. The previous equations were introduced for the nonlinear coherent directional coupler (NLDC) [2, 3], and they work well for dual-core fibers and for integrated couplers [4].

In the case of a birefringent optical fiber the XPM factor is $2/3$ and nonlinear four-wave mixing terms must be included, as well [5, 6, 7]:

$$
\begin{aligned}
& i\frac{da_x}{d\zeta} + \frac{1}{2}a_x + \left[|a_x|^2 + \frac{2}{3}|a_y|^2\right]a_x + \frac{1}{3}a_y^2 a_x^* = 0 \\
& i\frac{da_y}{d\zeta} - \frac{1}{2}a_y + \left[|a_y|^2 + \frac{2}{3}|a_x|^2\right]a_y + \frac{1}{3}a_x^2 a_y^* = 0
\end{aligned}
\tag{2}
$$

where $A_{x,y}$ are the complex envelopes of the fundamental modes polarized along the x,y principal axes of the fiber with propagation constants $\beta_{x,y}$, respectively. Moreover, $a_{x,y} \equiv \sqrt{\gamma/\Delta\beta}\exp\{-i(\beta_x+\beta_y)z/2\}A_{x,y}$, $\zeta = \Delta\beta z$ is a dimensionless distance, $\Delta\beta = \beta_x - \beta_y = 2\pi/L_b$ is the linear fiber birefringence and L_b the beat length. Let us express Eqs. 2 in a more compact form in terms of the circularly polarized components $a_\pm = (a_x \pm i a_y)/\sqrt{2}$ as

$$i\frac{da_+}{d\zeta} + \frac{1}{2}a_- + \frac{2}{3}\left[|a_+|^2 + 2|a_-|^2\right]a_+ = 0$$
$$i\frac{da_-}{d\zeta} + \frac{1}{2}a_+ + \frac{2}{3}\left[|a_-|^2 + 2|a_+|^2\right]a_- = 0 \quad (3)$$

At relatively low powers, fiber birefringence leads to the periodic exchange of power among the two circular polarizations: the spatial period of such linear coupling is equal to the linear beat length $L_b = 2L_c$ (L_c is the linear coupling length).

In order to better visualize the action of nonlinear coupling, it proves convenient to rewrite Eqs. 2 in terms of the real Stokes parameters $s_i \equiv S_i/S_0$, where $S_0 \equiv P = |a_x|^2 + |a_y|^2$, $S_1 \equiv |a_x|^2 - |a_y|^2$, $S_2 \equiv a_x a_y^* + c.c.$, and $S_3 \equiv -i a_x a_y^* + c.c.$:

$$\frac{ds_1}{d\zeta} = 2ps_2s_3$$
$$\frac{ds_2}{d\zeta} = -s_3 - 2ps_1s_3$$
$$\frac{ds_3}{d\zeta} = s_2 \quad (4)$$

where we defined the dimensionless input power $p \equiv P/P_c$, with the critical power level $P_c \equiv 3\Delta\beta/2\gamma$. In vector notation, Eqs. 4 can be written as

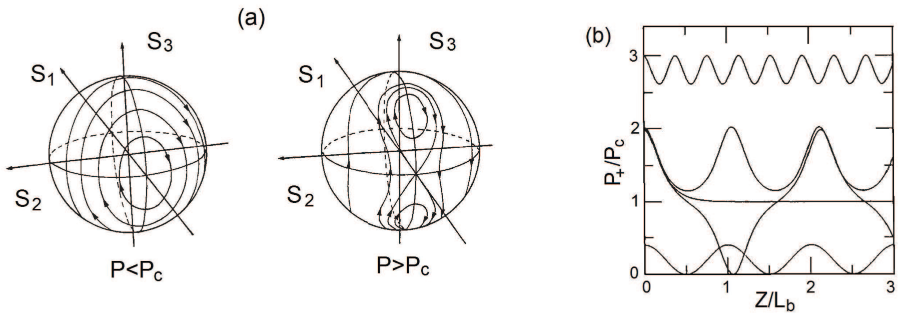

Fig. 1 (a): Poincaré sphere description of switching in a nonlinear coupler; (b) Evolution with distance of power in the input mode for different input power levels.

$$\frac{d\mathbf{s}}{d\zeta} = (\Omega_L + \Omega_{NL}(\mathbf{s}))\,\mathbf{s} \tag{5}$$

which describes polarization evolution on the Poincaré sphere as the motion of a rigid body subject to the sum of the fixed and the position-dependent angular velocities $\Omega_L \equiv (1,0,0)$ and $\Omega_{NL} = (0,0,-ps_3)$, respectively [6, 8]. Fig. 1(a) illustrates the radically different behavior of the polarization evolution trajectories of the tip of the Stokes vector $\mathbf{s}$ as the input power is below or above the critical power P_c. Below the critical power, all points on the Poincaré sphere rotate around the axis defined by Ω_L: as a result, the two circular polarizations periodically exchange their power along the fiber length. On the other hand, for $P > P_c$ the mode polarized along the fast axis of the fiber (i.e., whose Stokes vector is $\mathbf{s_F} = (-1,0,0)$) loses its spatial stability and becomes an unstable saddle (see right part of Fig. 1(a)) [6, 8, 9, 10]: as it is shown in Fig. 1(b), an input right-handed circular polarization (whose power is $P_+ \equiv |A_+|^2$) no longer periodically couples into the orthogonal left-handed polarization whenever $P_+ > 2P_c$.

2.2 Nonlinear Fiber Couplers

The NLDC is a basic device which permits all-optical routing and switching operations [2, 3]. Experiments have demonstrated nonlinear transmission and self-switching in fiber-optic NLDCs, such as: dual-core fibers [11]-[15], low birefringence fibers [16], and periodically twisted birefringent filters [17, 18]. Even though fiber optic NLDCs exhibit ultrafast nonlinear response, whenever their length $L \simeq L_b$, the associated switching power $P \simeq P_c$ is relatively high, owing to the weak nonlinearity of silica. Indeed, because of imperfections in fiber fabrication (in the case of dual core couplers) or of random fiber birefringence (for polarization couplers), beat lengths exceeding one or a few meters are not possible in practice. Earlier experiments with fiber NLDCs involved just one or two linear coupling distances L_c. In this case, the associated nonlinear transmission exhibits a single switching power, that is inversely proportional to L_c.

Nevertheless, full switching in a fiber NLDC of any length L is still possible when operating in the multi-beatlength regime, i.e., whenever $L >> L_b$ [19, 20]. The main advantage of the multi-beatlength NLDC is that the relevant switching power is inversely proportional to the total length of the fiber L. Therefore, the switching performance is comparable to that of other nonlinear fiber switches such as the nonlinear Mach- Zehnder interferometer (NMZI) and the nonlinear optical loop mirror (NOLM). Using a circularly polarized beam of power P at the input of a birefringent fiber, the exact solution of Eqs. 3 leads to the following expression for the output power P_+ in the same circular polarization

$$P_+ = \frac{P}{2}\left[1 + cn(\pi L/L_c|\tilde{p})\right] \tag{6}$$

where $\tilde{p} = p/2$ and cn is a Jacobi elliptic function. From Eq. 6, one obtains that the nonlinear period of polarization coupling between the two circular polarizations is

$$L_{nc}(\tilde{p}) = \frac{2L_c K(\tilde{p})}{\pi} \tag{7}$$

where K is the complete elliptic integral of the first kind. Whenever $\tilde{p} < 1$, one obtains that

$$K(\tilde{p}) = \frac{\pi}{2}\left[1 + \frac{\tilde{p}^2}{4} + O(\tilde{p})^2\right] \tag{8}$$

Therefore for $\tilde{p} << 1$ Eq. 6 reduces to

$$P_+ = P\cos^2(\pi L/2L_{nc}(\tilde{p})) \tag{9}$$

The associated on-off switching power p_s corresponds to the power-induced increase of the coupling distance which leads to a $\pi/2$ shift in the argument of the cosine in Eq. 9. One obtains $p_s = 2\sqrt{2L_b/L}$, i.e., in real units

$$P_s = \frac{12\pi}{\gamma\sqrt{2L_b L}} \tag{10}$$

The switching power of a fiber-based NLDC operating in the multi-beatlength regime may be further reduced by injecting an input elliptically (as opposed to circularly) polarized beam [21, 22]. Let us set $s_1(\zeta = 0) = \varepsilon\cos(2\phi)$, $s_1(\zeta = 0) = \varepsilon\sin(2\phi)$, and $s_3(\zeta = 0) = \sqrt{1-\varepsilon^2}$. From the exact solution of Eqs. 3, one obtains $P_+ = P(1 + s_3(L, p))/2$ for the right handed circular polarisation component at the output of a fibre of length L, where

$$s_3 = \sqrt{1 - \varepsilon^2\cos(2\phi)^2}\, f(p)\cos\left(2\pi r(p)L/L_b\right) \tag{11}$$

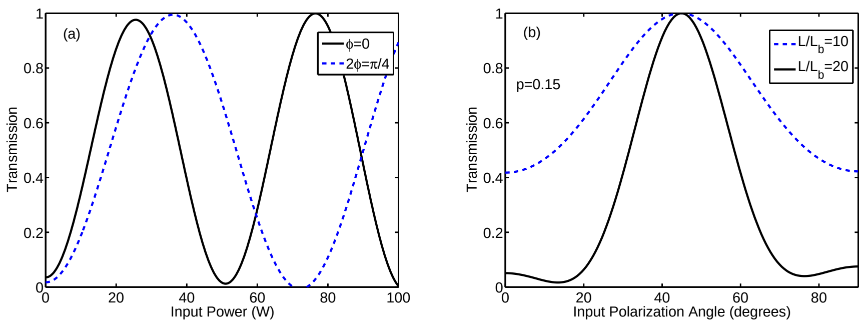

Fig. 2 Theoretical CW transmissions at the output of $L = 20L_b$ long birefringent fiber: (a) transmission dependence on input power for different input polarization angles; (b) transmission variation with input angle for two values of the total number of linear beat lengths L_b.

and $f(p) = (1 + p\varepsilon\cos(2\phi)/2)$. In this case, the nonlinear beat length $\tilde{L}_b(p) = L_b/f(p) \simeq L_b(1 - p\varepsilon\cos(2\phi)/2)$. By supposing $|cos(2\phi)| = 1$, the switching power p_s is defined by $2\pi(r(p)-1)L/L_b = \pi$, so that $p_s = L_b/\varepsilon L$. In real units, the switching power reads as

$$P_s = \frac{3\pi}{\gamma\varepsilon L} \tag{12}$$

In Fig. 2(a) we show an example of nonlinear CW transmissions computed from Eqs. 9 at the output of a $L = 20L_b$ long birefringent fiber. Here we plot the transmission dependence on input power for different input polarization angles ϕ, and we have set $\varepsilon = 0.37$, $\gamma L = 1$. As can be seen from Fig. 2(a), the switching power agrees well with the estimate $P_s \simeq 25$ W from Eq. 12. In Fig. 2 we also display the change of the nonlinear transmission as the input polarization angle ϕ is varied, for $L = 10 \div 20L_b$ and $p = 0.15$.

An experimental confirmation of all-optical power and polarization controlled switching in a multi-beatlength fiber NLDC was performed using 205 m of York ultralow-birefringence spun fiber [19]-[23]. The fiber was wound on a drum with radius of 15 cm, in order to introduce a bending-induced linear birefringence with $L_b \simeq 20$ m, so that $L \simeq 10L_b$. By increasing the input power of a right-handed circularly polarized beam from low values up to the switching power, an accumulated nonlinear variation of the beat length equal to L_c or 10 m (or 5% nonlinear variation per beat length L_b) was obtained.

Quasi-CW operating conditions were achieved using a mode-locked 100 ps input pulse train from an Nd-YAG laser operating at 1.06 μm. At the fiber output, the two circular polarization components of the emerging pulses were the two output chan-

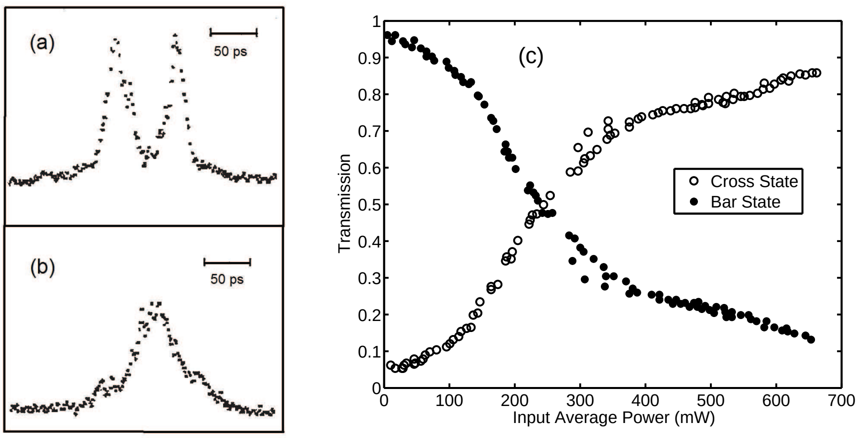

Fig. 3 Experimental pulse energy transmissions from orthogonal polarizations at the output of a 10 beat length long birefringent fiber: (a-b) streak-camera traces of pulses emerging from the input (bar state) and the orthogonal (cross state) polarizations; (c) average energy transmissions from cross and bar states versus input average power.

nels of the birefringent fiber NLDC. These components were separated by means of a calibrated Babinet-Soleil compensator, followed by a Wollaston prism.

Fig. 3(a-b) shows the streak camera pictures of the pulse profiles emerging from the bar (input) and the crossed circular polarizations components at the fiber output, for an input average power of 320 mW [19]. As it can be seen, the center and the wings of the pulse have opposite handedness, leading to a symmetric pulse breakup.

Fig. 3(c) shows the measured circular polarization transmissions at the fiber output, as a function of the input average power into the fiber [22]. Because of the slow response time of the photodetectors, the transmission displays the average power in each output polarization. At low powers, the input circular polarization emerges from the fiber almost unchanged. About 50% switching of the transmission is observed at about 250 mW: the corresponding peak pulse power is of about 20 W, in relatively good agreement with the estimate of Eq. 12, since in the experiment the condition $\gamma L \simeq 1$ is verified.

2.3 Nonlinear Mach-Zehnder Interferometers

A relatively simple nonlinear switch may be implemented using an all-fiber-based Mach-Zehnder interferometer (MZI): here two 3-dB linear directional couplers are used to split the input signal and then recombine the two arms of the interferometer of lengths L_1 and L_2, respectively (see Fig. 4). The components of the signal in the two arms of the MZI thus experience different overall linear and SPM induced phase shifts [24, 25, 27, 31]. The transmission through the bar port of the MZI reads as

$$T(P) = \sin^2(\Delta\phi_L + \Delta\phi_{NL}) \tag{13}$$

where $\Delta\phi_{NL} = \gamma P(L_1 - L_2)$. Alternatively, a different nonlinear phase shift in the two arms of the MZI may be induced whenever $L_1 = L_2$ by using an unbalanced linear directional coupler, so that the two signal components have different powers. A different implementation of a MZI type of switch consists of a highly birefringent

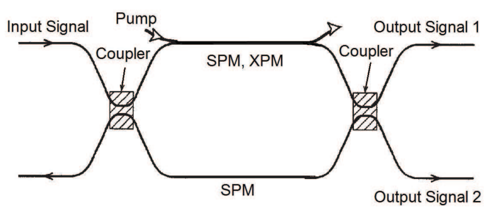

Fig. 4 Structure of a fiber based nonlinear MZ interferometer switch exploiting SPM or XPM (in the presence of a control pump).

fiber, where the two signal paths are represented by the two fiber modes which are orthogonally polarized along the principal axes of the fiber. For an input beam of power P that is initially linearly polarized with an orientation at the angle θ with respect to the $x-$axis of a birefringent fiber of length L, one has $P_x = P_0 \cos^2(\theta)$, $P_y = P_0 \sin^2(\theta)$, and $\Delta\phi_{NL} = \gamma PL \cos(2\theta)/3$.

Besides SPM-activated switching, a fiber MZI can be used to switch a signal among its two output ports through XPM by injecting a control pump at a different wavelength, that shifts the signal phase in the upper arm of the interferometer (see Fig. 4). In the presence of a control pump composed by a pulse train, the input CW signal may also be converted into a pulse train. The drawback of a fiber MZI is the presence of two separate paths for the signal, which make it sensitive to environmental perturbations, so that active stabilization of the fiber lengths may be required [25].

2.4 Nonlinear Loop Mirrors

The environmental stability of an interferometric fiber switch may be ensured by using a Sagnac loop configuration [28]-[33]: here the transmitted signal results from the coherent superposition at the directional coupler output port of two signals that have traveled in opposite directions around the same loop of fiber (see Fig. 5(a)). Clearly, whenever the directional coupler equally splits the input signal (i.e., a 3-dB coupler is used), there is no differential nonlinear phase shift among the two signal components that travel in opposite directions around the loop, and the Sagnac loop acts as a perfect mirror by reflecting all of the incoming signal: the transmitted signal vanishes. On the other hand, whenever an asymmetric coupler is used, there is a differential nonlinear phase shift which leads to a signal to be transmitted at high powers. Thus the Sagnac loop of Fig. 5(a) is also known as nonlinear loop mirror (NOLM).

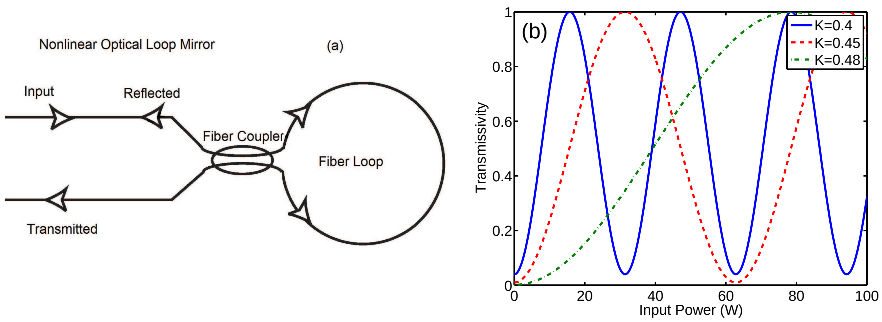

Fig. 5 (a) Structure of a fiber based NOLM and (b) associated power dependence of transmission for different power split coefficients K of the coupler.

The nonlinear transmission of the NOLM can be simply obtained as follows. The input amplitude of the waves traveling clockwise and counter-clockwise in the loop reads as $A^i_{CW} = \sqrt{K}A_{in}$ and $A^i_{CCW} = i\sqrt{1-K}A_{in}$, respectively, where K is the power splitting ratio of the coupler and A_{in} is the input signal amplitude. After one round-trip through the loop, the two fields traveling in opposite directions acquire equal linear but different nonlinear (as determined by both SPM and XPM) phase shifts, so that at the input of the coupler one has the two fields

$$\begin{aligned} A^o_{CW} &= A^i_{CW} \exp\left\{i\beta L + i\gamma\left(|A^i_{CW}|^2 + 2|A^i_{CCW}|^2\right)L\right\} \\ A^o_{CCW} &= A^i_{CCW} \exp\left\{i\beta L + i\gamma\left(|A^i_{CCW}|^2 + 2|A^i_{CW}|^2\right)L\right\} \end{aligned} \tag{14}$$

where β is the linear propagation constant in the fiber loop of length L. At the coupler output, one obtains $A_t = \sqrt{K}A^o_{CW} + i\sqrt{1-K}A^o_{CCW}$, so that the transmissivity of the NOLM reads as

$$T(P) \equiv |A_t|^2/|A_i|^2 = 1 - 4K(1-K)\,cos^2\left[(K-0.5)\,\gamma P_{in}L\right] \tag{15}$$

where $P_{in} = |A_{in}|^2$. The resulting input signal power dependence of the NOLM transmissivity is illustrated in Fig. 5(b) for different values of the coupling ratio K, and for $\gamma L = 1$. The associated switching power (corresponding to the first unit peak of the transmissivity as P is increased from zero) reads as

$$P_s = \frac{\pi}{\gamma L(1-2K)} \tag{16}$$

which leads to $P_s \simeq= 16W$ and $P_s \simeq= 31W$ for $K = 0.4$ and $K = 0.45$, respectively (see Fig. 5(b)).

As in the nonlinear MZI, signal switching in the NOLM may also be induced via XPM by injecting in the loop, by means of a directional coupler, a pump pulse at a different wavelength (see Fig. 6(a)) [34]-[37]. The control pulse propagates in the CCW direction, thus it only induces a nonlinear phase shift into the corresponding

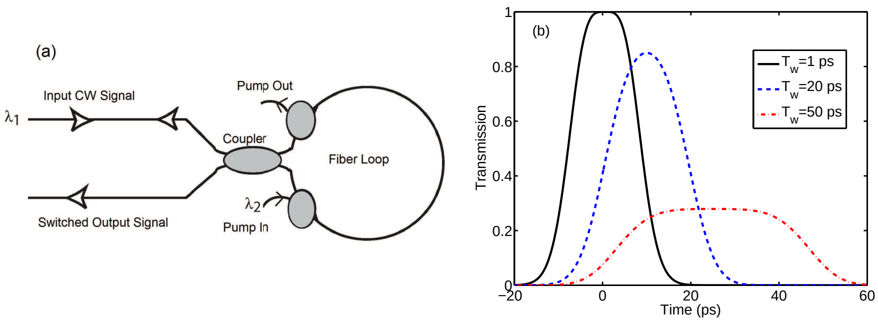

Fig. 6 (a) Schematic of XPM-controlled switching in a NOLM and (b) transmission function for $T_0 = 10ps$ and different values of the walk-off time T_w.

component of the signal, so that propagation in the NOLM is un-balanced even when $K = 0.5$. In this case, the NOLM acts as a perfect reflecting mirror for a signal in the absence of the control pump, whereas in the presence of the pump the signal may be fully transmitted. For evaluating the nonlinear phase shift induced via XPM on the signal by a short pump pulse, one should take into account the temporal walk-off between pump and signal due to fiber GVD. The total XPM phase shift is

$$\Delta\phi(T) = 2\gamma\int_0^L |A_p(T - \delta x)dx, \tag{17}$$

where T is time in the reference frame that moves with the group velocity at the signal wavelength V_s, and $\delta = V_p^{-1} - V_s^{-1}$ is the group velocity mismatch between pump and signal. For a Gaussian pump pulse of the form $A_p(T) = P\exp\left(-T^2/T_0^2\right)$ (so that the pump pulse full width at half maximum is $T_{fwhm} \simeq 1.66T_0$), the resulting nonlinear phase shift reads as

$$\Delta\phi(T) = \frac{\gamma LP\sqrt{\pi}T_0}{T_w}\left[erf\left(\frac{T}{T_0}\right) - erf\left(\frac{T-T_w}{T_0}\right)\right], \tag{18}$$

where $erf(x)$ is the error function, and the total walk-off is $T_w = \delta L$. The associated nonlinear signal transmission is

$$T = 1 - 4K(1-K)\cos^2(\Delta\phi/2), \tag{19}$$

Let us consider a balanced coupler with $K = 0.5$, a peak XPM-induced phase shift $2\gamma LP = \pi$, and set $T_0 = 10$ps. Fig. 6(b) shows examples of signal transmission windows for different values of the walk-off time T_w. As it can be seen, whenever $T_w << T_0$ the transmission window is a replica of the control pulse; whereas as soon as $T_w > T_0$ the peak value of the transmission drops from unity and the window broadens in time.

2.5 Nonlinear Passive Loop Resonators

A variant of the nonlinear Sagnac interferometer is provided by the nonlinear fiber ring resonator [38, 39, 40, 41, 42]. As an example, consider the scheme of Fig. 7(a): instead of connecting the two output ports of the coupler, a fiber loop now connects the first output port (port 3 in Fig. 7(a)) with the second input port (port 2) of the coupler. The signal E_1 at input port 1 enters the coupler and it continuously recirculates in the loop; the cavity field can be monitored at the second output port (port 4) of the coupler. The complex amplitude transmission $Y = A_4/A_1$ of the ring resonator is obtained from the relations $A_3 = \sqrt{1-\tau}(\sqrt{1-K}A_1 + i\sqrt{K}A_2)$ and $A_4 = \sqrt{1-\tau}(i\sqrt{K}A_1 + \sqrt{1-K}A_2)$, where τ is the fractional power loss of the coupler and $A_2 = A_3\exp(-\alpha L + i\beta L + i\Delta\phi_{NL})$ with $\Delta\phi_{NL} = \gamma|A_3|^2L$. The result is provided by the implicit equation

$$Y = \frac{(1-\tau)\exp(i\delta - \alpha L) + i\sqrt{1-\tau}\sqrt{K}}{1 - i\sqrt{K}\sqrt{1-\tau}\exp(i\delta - \alpha L)}, \tag{20}$$

where

$$\delta = \beta L + \gamma|A_1|^2 L\left(\frac{1-\tau}{1-K} + \frac{K}{1-K}|Y|^2 + i\frac{\sqrt{K}\sqrt{1-\tau}}{1-K}(Y - Y^*)\right), \tag{21}$$

Clearly Eq. 20 is equivalent to two real equations, whose numerical solution yields the power transmissivity $T = |A_4|^2/|A_1|^2$ of the nonlinear resonator (see Fig. 7(b), where the resonant coupling coefficient is $M = (1-\tau)\exp(-\alpha L) = 0.95$). As it can be seen, by varying the linear phase delay βL right below the resonance condition $\beta L = 3\pi/2 + 2\pi m$ (where m is an arbitrary integer), one obtains quite different nonlinear transmission behaviors. For small detunings from resonance (i.e., $\beta L = 1.49\pi$), it is only necessary to add a weak nonlinear phase shift (of the order of $\pi/100$) in order to bring the resonator back into resonance. At higher input powers, the resonator gets out-of-resonance and transmissivity rapidly increases. On the other hand, for larger linear cavity detunings (e.g., for $\beta L = 1.45\pi$), the transmissivity becomes multi-valued, and optical multistability results: again, the on-off switching power is relatively low, i.e., it is obtained for nonlinear phase shifts $\gamma|A_3|^2 L \simeq \pi/100$, which is accessible at CW signal power levels.

2.6 Optical Soliton Switching

As we have seen in Sect. 2.1, the efficiency of all-optical switching in nonlinear couplers using optical pulses is severely limited unless square pulses (e.g., the non-return-to-zero (NRZ) data modulation format) are used [15]. In fact, the CW transmission curve is effectively averaged over the pulse profile, and pulse

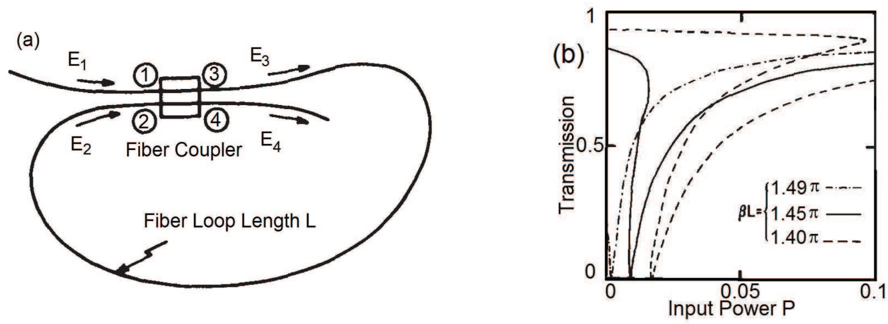

Fig. 7 (a) Schematic passive fiber loop resonator and (b) its transmissivity for different values of βL; here $K = 0.95$.

break-up occurs at the device output, since different portions of the pulse profile are independently switched according to their instantaneous power level (see Fig. 3(a,b)); the same occurs with nonlinear inteferometers. The pulse break-up effect may be avoided by operating in the soliton regime, that is whenever the signal pulses represent optical fiber solitons for the fibers used in the switching device [24, 32, 33, 43, 44, 45]. In the short pulse regime, the equations describing propagation in a nonlinear coupler should be extended to include group velocity dispersion terms, which leads to the coupled nonlinear Schrödinger equations

$$
\begin{aligned}
i\frac{\partial u}{\partial \xi} + \frac{\beta}{2}\frac{\partial^2 u}{\partial \tau^2} + \kappa v + \left(|u|^2 + \rho |v|^2\right) u = 0 \\
i\frac{dv}{d\xi} + \frac{\beta}{2}\frac{\partial^2 v}{\partial \tau^2} + \kappa u + \left(|v|^2 + \rho |u|^2\right) v = 0
\end{aligned}
\tag{22}
$$

where the dimensionless distance is $\xi = z|\beta_2|/t_s^2$, β_2 is the GVD coefficient, $\beta = \pm 1$ for anomalous or normal dispersion, respectively, $\tau = z/t_s$ where t_s is a reference pulse width. Moreover, the dimensionless coupling coefficient $\kappa = Ct_s^2/|\beta_2| = P_c/2P_{sol}$, where $P_c = 2C/\gamma$ is the NLDC critical power, $P_{sol} = |\beta_2|/\gamma t_s^2$ is the soliton power, and ρ is the XPM coefficient.

Fig. 8(a,b) illustrates beam propagation solutions of Eqs. 22 in the anomalous GVD regime. Here $\gamma = 0$ (as in a linear dual-core fiber coupler) and $\kappa = 1/4$. As it can be seen, input soliton-like pulses of the form $u(0,\tau) = u_0 sech(\tau/\tau_0)$ (here $v(0,\tau) = 0$ and $\tau_0 = 1$) are entirely switched as a single entity from the cross to the bar output state as the input soliton peak power $p = |u_0|^2/P_c$ is increased from $p = 2$ to $p = 3$. For $p = 2$, the input pulse periodically couples back and forth

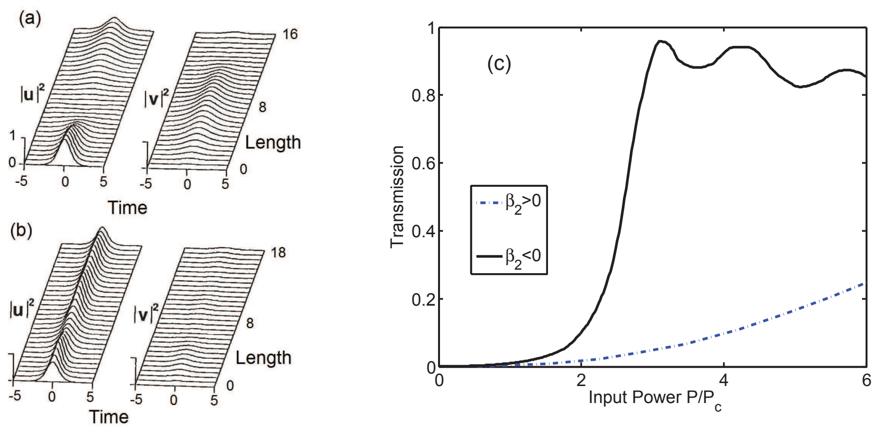

Fig. 8 Evolution of power with distance in the bar and cross state of soliton NLDC at (a) low and (b) high powers; (c) comparison of power-dependent transmission in the bar state for dispersive pulses in the anomalous (solid curve) and normal (dashed curve) dispersion regime.

between the two channels, with a relatively small distortion of the pulse profile. Whereas for $p = 3$ the soliton transfer between the channels is inhibited. Therefore optical solitons exhibit a particle-like switching behavior, and the pulse break-up which is observed in the absence of GVD (or for quasi-CW input signals) may thus be avoided.

Fig. 8(c) compares the fraction of energy transmitted in the bar state as a function of the input peak power p, when using a NLDC in either the anomalous ($\beta > 0$) or normal ($\beta < 0$) GVD regime, respectively. Here we have chosen $\kappa = \pi/2$, and $\tau_0 = 1/\sqrt{2\pi}$, so that twice the CW critical power is equal to the fundamental soliton peak power. As it can be seen, with normal GVD the dispersive pulse broadening combined with SPM and linear coupling nearly inhibits the self-switching behavior. Conversely, in the anomalous GVD regime, the transmission is similar to that obtained for CWs or ideal square pulses (besides an increase of the effective switching power).

3 Optical Switching in Integrated Optical Waveguide Structures

3.1 All-Optical Switching in Photonic Crystal Couplers

In recent years Photonic Crystals (PC) have received increasing attention from the scientific community, especially for their ability to control the propagation of light [46]. The basic building blocks for all-optical data processing such as waveguides with sharp bends, high-Q resonant cavities, perfect mirrors and so on could indeed be integrated on a single PC chip, in order to achieve complex functions with high performance and small size [47]. PC structures seem to be the ideal choice to get efficient nonlinear devices for optical switching, because of the strong confinement of the fields that permits to optimize the nonlinear interactions. In particular, the development of nonlinear PCs exploiting the ultrafast Kerr nonlinearity has become an important issue. The feasibility of bistable switching devices [48], optical diodes and nonlinear bends [49], and optical isolators [50] has been reported. Directional couplers are fundamental components for optical networks, and it has been demonstrated that PC couplers exhibit smaller size and better performance than the conventional ones [51]-[53]. Here we describe the properties of an all optical switch based on an ultrashort PC coupler. Switching is performed by exploiting the strong Kerr nonlinearity of AlGaAs, by controlling the intensity of the input signal. The reported two-dimensional finite-difference time-domain (2D FDTD, [54, 55]) analysis shows that the resulting ultra-compact device is characterized by a switching power comparable with the one reported in the literature for centimeter-long conventional nonlinear directional couplers.

The schematic view of the proposed structure is shown in Fig. 9. The PC is formed by a square lattice of AlGaAs rods in air. AlGaAs seems to be a proper material since it has a large nonlinear refractive index, with minimal linear and nonlinear absorption in the 1550 nm telecommunications window [56]. The PC lattice constant is $a = 400$ nm, whereas the radius of the rods for the bulk crystal is $r = 130$ nm. The resulting structure has a wide bandgap for TM polarization in a range of wavelengths between 1400 and 1750 nm. Two waveguides are formed by introducing linear defects reducing the radius of the rods to $r_{dif} = 70$ nm [57]. The reason for this choice is twofold. First, single-mode waveguides are essential to get a directional coupler, with only one even and one odd supermode. It is well known that reduced-index waveguides satisfy this requirement, whereas the increased-index ones tend to be multimode [57]. Second, the need to optimize the nonlinear interactions suggests to reduce only partially the radius of the defect rods, in order to maximize the semiconductor fill factor. We have calculated that in the previously described guiding structure over 50% of the modal field energy is confined into the nonlinear dielectric defects [58]. The correct design of the coupler section is the key point for our problem. We have found that the critical parameter to achieve switching with reasonable input intensity of the light is the distance between the two waveguides. Therefore fully vectorial eigenmodes of Maxwell's equations for a set of couplers were computed using a freely available mode solver [58], and 2D FDTD simulations [54, 55] were analyzed to study the device behavior when the waveguides separation is varied.

Moreover, a very simple and powerful coupled-mode theory was developed to model nonlinear propagation in PC couplers. As expected, there is a tradeoff between length of the structure and switching intensity. If the waveguides are close to each other the linear coupling is strong, thus it is very difficult to decouple them exploiting the effects of the ultrafast Kerr nonlinearity. If the waveguides are far away, the beat length of the coupler is very large, and the resulting device is not ultra-compact. We have then chosen a coupler composed of two waveguides separated by five lattice constants, as shown in Fig. 9. In Fig. 10 we report the projected band structure of the coupler, evaluated through the mode solver [58]. It is straightforward to calculate the beat length $L_B = 2\pi/(k_{even} - k_{odd})$ of the device, which

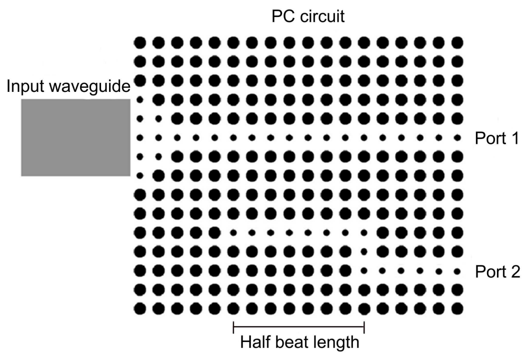

Fig. 9 Schematic view of the PC structure. $L_B = 140\ \mu$m is the beat length of the coupler. It is worth to note that the real length is scaled to fit in the figure.

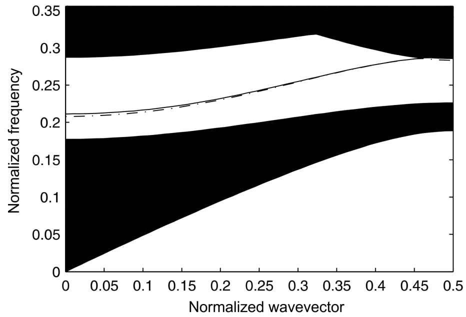

Fig. 10 Projected band structure of the coupler, with the normalized dispersion relations for the odd (solid line) and the even (dash-dotted line) supermode. Note that in our case we are working around $a/\lambda = 0.256$.

is about 140 μm at the wavelength λ = 1560 nm; k_{even} and k_{odd} are the effective wavenumbers of the even and the odd supermode. Light can be coupled from a dielectric slab waveguide (width W = 3 μm) to the coupler through a tapered input section [59], as shown in a schematic way in Fig. 9. More complex and efficient PC tapers have been proposed (e.g. in Ref. [60]), nevertheless a systematic analysis of the input section of the PC chip in order to optimize the coupling efficiency is well beyond the aim of this section. The switch layout is completed with the double sharp bend that decouples the two waveguides just in proximity of the half beat length of the coupler (see Fig. 9). The final structure, composed of the tapered input section, the coupler and the double sharp bend is about 75 μm long.

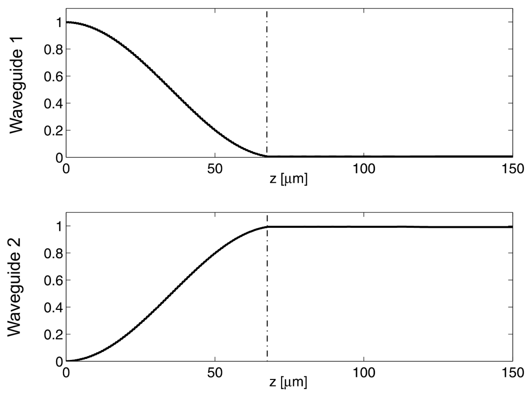

Fig. 11 Normalized intensity of the field in WG_1 (at the top) and WG_2 (on the bottom) in linear regime ($\gamma_n = 0$) calculated through the coupled defects model. The sharp bend is placed near the defect $n = 170$ (see the dash-dotted line).

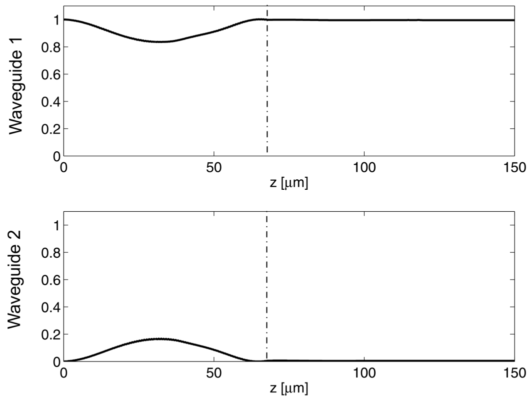

Fig. 12 Normalized intensity of the field in WG_1 (at the top) and WG_2 (on the bottom) in nonlinear regime ($\gamma_n |a_{in}|^2 = 0.75\ s^{-1}$) calculated through the coupled defects model. The sharp bend is placed near the defect $n = 170$ (see the dash-dotted line).

In order to show the basic operation principle of the proposed structure we exploit a coupled-mode theory [61]-[63], developed to study coupled defects in nonlinear PCs. In case of weak interactions between similar single-mode defects, the modal field of each defect can be considered unperturbed, so that only the field amplitudes vary in time. The evolution of the state of each PC waveguide, considered as a straight chain of resonators, is governed by a set of differential equations

$$i\frac{da_n}{dt} + C_n\left(a_{n+1} + a_{n-1}\right) + \gamma_n \left|a_n\right|^2 a_n = 0 \tag{23}$$

where a_n is the field amplitude in the n-th defect, C_n is the nearest-neighbor linear coupling coefficient and γ_n is the self-phase modulation strength [61]-[63]. This theory was proposed for the analysis of propagation in coupled-resonator optical waveguides (CROW). In our case, the individual defect rods composing the linear defect are strongly coupled, therefore the accuracy of the model could be questionable. Nevertheless, we show that this rough and simple theory can help to understand the behavior of the nonlinear PC coupler. We can introduce the coupling between the two waveguides just defining two sets of equations

$$i\frac{da_n}{dt} + C_n\left(a_{n+1} + a_{n-1}\right) + D_n \cdot b_n + \gamma_n \left|a_n\right|^2 a_n = 0 \tag{24}$$

$$i\frac{db_n}{dt} + C_n\left(b_{n+1} + b_{n-1}\right) + D_n \cdot a_n + \gamma_n \left|b_n\right|^2 b_n = 0 \tag{25}$$

where a_n and b_n are the field amplitudes in the n-th defect of the first and the second waveguide (called WG_1 and WG_2 respectively), and D_n is the linear coupling coefficient between the n-th defect in the first and in the second waveguide. We have solved numerically the system composed of Eqs. (24) and (25) in the linear regime ($\gamma_n = 0$). The coupling coefficient C_n was fixed to $2\ s^{-1}$ for every n, whereas

$D_n = 0.035\, s^{-1}$ for $n < 170$ and $D_n = 0$ elsewhere, in order to simulate the introduction of the double sharp bend. Fig. 11 shows that the coupled-defect theory is able to reproduce the behavior of the PC coupler. We report the calculated values of a_n and b_n for a CW excitation when a steady-state is reached. The input field is injected into WG_1, and the field flows toward WG_2 because of the linear coupling between the two waveguides. The sharp bend is in proximity of the half beat length of the coupler, thus at the output all the optical energy is in WG_2. In Fig. 12 we report the numerical solution of the system composed of Eqs. 24 and 25 in nonlinear regime ($\gamma_n\, |a_{in}|^2 = 0.75\, s^{-1}$). It is straightforward to note the effect of the nonlinearity: now at the output all the optical energy is in WG_2, which shows that it is possible to switch the output channel by varying the input field intensity.

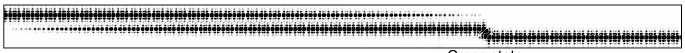

Fig. 13 Intensity of the field in the PC coupler with maximum input intensity 1 GW/cm^2: the coupler is in cross state, the power ratio is about 20 dB.

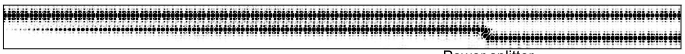

Fig. 14 Intensity of the field in the PC coupler with maximum input intensity 3.8 GW/cm^2: the coupler behaves as a 50% power splitter, the power ratio is about 0 dB.

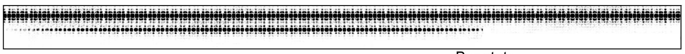

Fig. 15 Intensity of the field in the PC coupler with maximum input intensity 5 GW/cm^2: the coupler is in bar state, the power ratio is about -20 dB.

Now we show a rigorous 2D FDTD analysis of the feasibility of all-optical switching in the previously described device. The problem of the implementation of the structure on a real PC slab is a big issue that would require huge 3D FDTD simulations, in order to estimate scattering losses in the third dimension. We highlight that the 2D numerical modeling of the real 3D device is commonly used in the literature for the study of phenomena due to Kerr effect in PC (see Refs. [48]-[50]), since this permits to focus the attention mainly on the nonlinear interactions. The nonlinear PC coupler is simulated by injecting into the taper section a CW Gaussian field that approximates the fundamental mode of the dielectric slab waveguide. It is worth to note that in this way we take into account of the effects due to the coupling efficiency into the PC chip. By varying the maximum value of the Gaussian, and then the related maximum intensity of the input light, we can characterize the behavior of the power-controlled switch.

In Figs. 13-15 we show the intensity of the electromagnetic field in the device for three different intensities of the input signal. Fig. 13 shows the simulation result for a maximum input intensity $I_{INmax} = 1\ GW/cm^2$. It is possible to see that all the optical energy flows through the output port 2, thus the coupler is in cross state. This behavior is in good agreement with the previously described design procedure, in fact the double sharp bend decouples the two waveguides just near the half beat length. In Fig. 14 we have increased the maximum input intensity to $I_{INmax} = 3.8\ GW/cm^2$. Here it is clear the effect of the nonlinear phase shift: the input intensity is equally divided between the two output waveguides, and the structure behaves as a 50% power splitter. Fig. 15 shows the behavior of the device increasing I_{INmax} to 5 GW/cm^2. In this case all the optical energy flows through the output port 1, thus the coupler is in a bar state induced by the nonlinearity. It is worth pointing out that the result of the FDTD simulation shown in Fig. 15 is in agreement with the solution of the coupled defects model (see Fig. 12). The field injected in WG_1 initially couples to WG_2 as in an asymmetric coupler, but at the double sharp bend position all the optical energy is in WG_1, as desired. Fig. 16 summarizes the operation principle: a high-intensity signal propagates along the input waveguide and flows through the output port 1, whereas a low-intensity signal is switched toward output port 2.

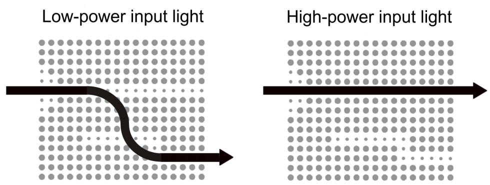

Fig. 16 The power-controlled switching function: a low-intensity signal is switched toward output port 2 (linear coupler), whereas a high-intensity signal propagates along the input waveguide because of the nonlinear phase shift.

In Fig. 17 we show the power ratio in decibel, i.e. the ratio between the optical energy in the output ports 2 and 1 of the structure, versus the maximum value of the input intensity at $\lambda = 1555$ nm, $\lambda = 1560$ nm and $\lambda = 1565$ nm, respectively. The simulations demonstrate that the device can be considered an optically-controlled switch, with a power ratio larger than 20 dB in a wide range of wavelengths. In presence of pulsed excitations the performance of the power-controlled switch decrease with respect to the CW case. In particular, as has already been described in Sect. 2, with nonsquare input pulses the power ratio is reduced and output pulse break-up is observed [64, 65]. Nevertheless these phenomena are strongly dependent on the shape and the duration of the pulses, and they do not affect the validity of the proof-of-principle nonlinear PC coupler. It is interesting to compare the device behavior with what has already been reported in the literature for NLDCs made by AlGaAs

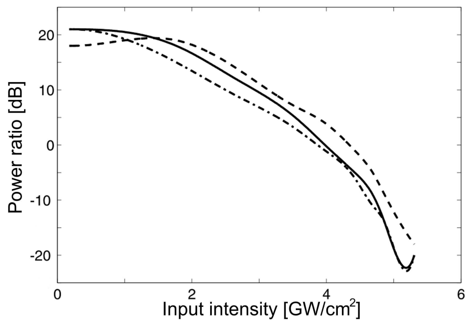

Fig. 17 Power ratio versus maximum input intensity of the light at λ = 1560 nm (solid line), λ = 1555 nm (dash-dotted line) and λ = 1565 nm (dashed line).

semiconductor waveguides, and operating in the third-telecommunications window. In this second case, both simulations and experiments show switching powers from 50 to 90 W, for a few centimeters long devices [64, 65]. Assuming that the field at the input of the PC chip is a Gaussian beam, with the same spot-size $w_0 = 1\ \mu$m we used in the 2D FDTD simulations, we can integrate the input intensity finding an approximated power for the total switching of about 70 W, which is comparable with the previously given values. Nevertheless, it is fundamental to note that the length of the nonlinear PC coupler is less than 80 μm, which is significantly shorter than standard waveguide NLDCs. The one-pulse scheme analyzed throughout the paper could be extended to a pump signal configuration, with a strong pump acting through cross-phase modulation (XPM) on a weak signal at different wavelength.

3.2 Graphene-Assisted Control of Coupling Between Surface Plasmon Polaritons

We discuss in this Section the tuning of the coupling of surface plasmon polaritons between two graphene layers with nanometer spacing. We demonstrate that, by slightly changing the electrical doping and then shifting the chemical potential, a graphene coupler can switch from the bar to the cross state. As a consequence, the coupling coefficient in such structures can be easily controlled in an ultrafast fashion either by means of an applied electrical signal [66] or by changing the intensity of the signal at the device input. These findings open the way to fully exploit the huge nonlinearity of graphene for all optical signal processing: from one side giving more degrees of freedom to already proposed devices [67, 68, 69, 70, 71], from the other side paving the way to new devices.

Graphene can sustain surface plasmon polaritons (SPP) having unique properties as compared to what we are used to with noble metals. In fact a single layer of graphene can support either TE or TM polarized plasmons without suffering from huge loss [72, 73, 74]; moreover, as far as TM polarization is concerned, the extremely high confinement factor is particularly favourable to explore the huge $\chi^{(3)}$ nonlinearity of graphene [67, 75, 76]. Experimental endeavors have demonstrated the evidence of graphene plasmons by measuring the plasmon resonance of graphene nanoribbon arrays [77], and by acquiring their near field images [78, 79]. The coupling of SPP between separated graphene layers has been recently analyzed in [80]; however the very interesting properties arising from the easily tunable optical properties of graphene have not been exploited yet in this framework. Here in particular we show that by slightly changing the chemical potential, a graphene coupler can switch from the bar to the cross state.

In Fig. 18 we report the basic geometry that we are going to consider in this section; two graphene layers are embedded in a dielectric structure: region 1 (of width $2s$) is the dielectric in between the two graphene layers. At the graphene boundary we set the following conditions on the tangential components of the electromagnetic field:

$$
\begin{aligned}
(\mathbf{E}_{2,3} - \mathbf{E}_1) \times \hat{x} &= 0 \\
(\mathbf{H}_{2,3} - \mathbf{H}_1) \times \hat{x} &= \pm i\omega\varepsilon_0\varepsilon_{rS1-2,3}\mathbf{E}_{\parallel}(x = \pm s)
\end{aligned}
\tag{26}
$$

where $\mathbf{E}_{\parallel}$ is the electric field tangent to the graphene layer and ε_{rS1-2} (ε_{rS1-3}) is the relative surface permittivity of the graphene layer between regions 1 and 2 (3). As far as the electromagnetic constants of graphene are concerned, we write the linear contribution to the relative complex permittivity as [81, 82]:

$$
\varepsilon_{rC} = \frac{\varepsilon_{rS}}{d_g} = 1 + \frac{\sigma^{(1)}_{\Sigma,I}}{d_g\omega\varepsilon_0} - i\,\frac{\sigma^{(1)}_{\Sigma,R}}{d_g\omega\varepsilon_0} = \varepsilon_{rC,R} + i\varepsilon_{rC,I} \tag{27}
$$

where d_g is the graphene thickness and the surface complex conductivity $\sigma^{(1)}_{\Sigma} = \sigma^{(1)}_{\Sigma,R} + i\sigma^{(1)}_{\Sigma,I}$ (in Siemens) is obtained from theoretical models now well established and experimentally validated [82], which give the following dependence of the real and imaginary parts of the conductivity on frequency (ω), temperature (T) and chemical potential (μ):

$$
\begin{aligned}
\sigma^{(1)}_{\Sigma,\mathrm{R}}(\omega) &\simeq \frac{\sigma_0}{2}\left(\tanh\frac{\hbar\omega + 2\mu}{4k_BT} + \tanh\frac{\hbar\omega - 2\mu}{4k_BT}\right) \\
\sigma^{(1)}_{\Sigma,\mathrm{I}}(\omega) &\simeq \frac{\sigma_0}{\pi}\left[\frac{4}{\hbar\omega}\left(\mu - \frac{2\mu^3}{9t^2}\right) - \log\frac{\hbar\omega + 2\mu}{\hbar\omega - 2\mu}\right]
\end{aligned}
\tag{28}
$$

where $t = 2.7$eV is the hopping parameter, $\hbar$ and k_B are the reduced Planck's and Boltzmann's constants, respectively, and $\sigma_0 = e^2/(4\hbar) \simeq 6.0853 \cdot 10^{-5}$ S, with e the electron charge.

Note also that this model can be easily extended into the nonlinear regime by adding a nonlinear correction to the surface conductivity as: $\sigma_{\Sigma} = \sigma^{(1)}_{\Sigma} + \sigma^{(3)}_{\Sigma}|\mathbf{E}|^2E_{y,z}$ [73]. Moreover, thanks to the extremely small thickness of the graphene layer, nonlinearity can be analyzed by introducing a parameter embedded into the coefficients describing the continuity of the tangential components of the electromagnetic field [67, 76].

To describe SPP propagation along z, we first note that, at first order, the y dependence of the electromagnetic field can be neglected; we then look for guided modes with harmonic temporal dependence $\exp(i\omega t)$ and spatial variation $\mathbf{E}_{1,2,3}(x,z)$, $\mathbf{H}_{1,2,3}(x,z) \sim \exp(-i\beta z \pm \Gamma_{1,2,3}x)$ with $= \Gamma^2_{1,2,3} = \beta^2 - \varepsilon_{r1,2,3}k_0^2$. Obviously the complex wavenumber β, through its real and imaginary parts, describes the evolution of both the phase and the amplitude of the guided modes. We can apply the above modeling to derive the dispersion relation of both TE and TM modes. In the following we describe in details the TM polarization. We first consider a very general situation where the two graphene layers can be biased in a different way to give rise to an asymmetric coupler. After straightforward algebra we find that coupled SPP in the system are determined by setting to zero the determinant of the following matrix:

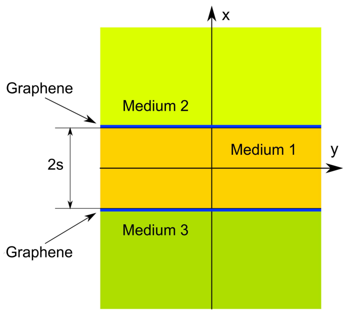

Fig. 18 Schematic of the graphene directional coupler: the separation between the layers is equal to $2s$.

$$M = \begin{bmatrix} e^{\Gamma_1 s} & e^{-\Gamma_1 s} & -e^{-\Gamma_2 s} & 0 \\ e^{-\Gamma_1 s} & e^{\Gamma_1 s} & 0 & -e^{-\Gamma_3 s} \\ \frac{i\omega\varepsilon_1}{\Gamma_1}e^{\Gamma_1 s} & -\frac{i\omega\varepsilon_1}{\Gamma_1}e^{-\Gamma_1 s} & g_{1-2}e^{-\Gamma_2 s} & 0 \\ -\frac{i\omega\varepsilon_1}{\Gamma_1}e^{-\Gamma_1 s} & \frac{i\omega\varepsilon_1}{\Gamma_1}e^{\Gamma_1 s} & 0 & g_{1-3}e^{-\Gamma_3 s} \end{bmatrix} \quad (29)$$

where g_{1-2} and g_{1-3} take into account the contribution of the two graphene layers in the continuity conditions:

$$g_{1-2} = i\omega\varepsilon_0\varepsilon_{rS,1-2} + \frac{i\omega\varepsilon_2}{\Gamma_2}, g_{1-3} = i\omega\varepsilon_0\varepsilon_{rS,1-3} + \frac{i\omega\varepsilon_3}{\Gamma_3}$$

where $\varepsilon_{rS,1-2}$ and $\varepsilon_{rS,1-3}$ refer to the relative dielectric constant of the two graphene layers, which in general may have different values due to different carriers concentrations. This asymmetric coupler offers a wide variety of possible settings which certainly deserve to be investigated both in the linear and in the nonlinear regime. Here we describe a prototype example into the possibilities offered by the tunability of graphene parameters in this framework; we thus focus our attention on a very particular situation corresponding to a linear and symmetric case ($\varepsilon_2 = \varepsilon_3$ and $\varepsilon_{rS,1-2}$=$\varepsilon_{rS,1-3}$); moreover we use $T = 300K$ and $\lambda = 10$ μm. For the sake of simplicity, we also set $\varepsilon_{r1} = \varepsilon_{r2} = \varepsilon_{r3} = 2.25$. In this regime the graphene directional coupler has two different eigenstates: the even (odd) supermode corresponding to the out of phase (in phase) hybridization of the SPP guided by the single graphene layers. Note also that the even mode here has always the highest value of the propagation constant.

In Fig. 19 we report the solution of the dispersion relation as a function of s for two different situations: continuous lines here refer to the even and odd supermodes corresponding to a chemical potential $\mu_1 = 0.1$ eV in Eqs. 28, while the dashed lines refer to a choice of the chemical potential $\mu_2 = 0.15$ eV in Eqs. 28. It is straight-

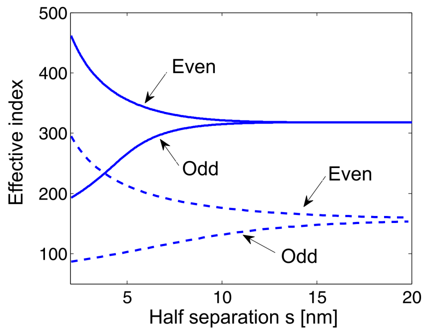

Fig. 19 Effective index $n_{eff} = \Re e(\beta)/k_0$ of even and odd supermodes of the coupled graphene layers as a function of the separation among the layers. Continuous (dashed) lines refer to a chemical potential of $\mu_1 = 0.1$ eV ($\mu_2 = 0.15$ eV).

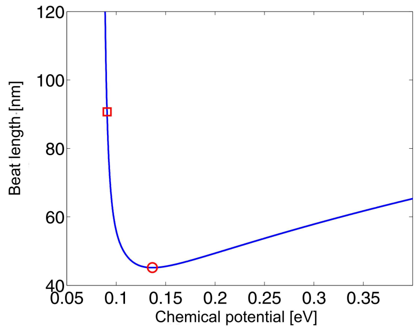

Fig. 20 Beat length versus chemical potential for a graphene plasmon coupler. Here $2s = 10nm$.

forward to note that, for large enough s, the two supermodes of the coupler tend to degeneracy, and their propagation constants approximate the propagation constant of the SPP of a single graphene layer. The main message we can read from Fig. 19 is that a very small change in the chemical potential can induce a very big change in the behaviour of the coupler. In the following, we focus our attention to the case with $s = 5nm$. For this value of the separation between the layers, we computed the beat length of the directional coupler as a function of the chemical potential: the corresponding results are reported in Fig. 20. We can clearly see there that a very small change of the chemical potential can be used to induce huge changes of the beat length of the coupler. The two particular points (open square and open circle) enlightened in Fig. 20 are the initial conditions in Fig. 21, where we describe the propagation of the electromagnetic signal in the graphene coupler. In both panels in Fig. 21 total propagation length is set to $L \simeq 90nm$. On the left panel in Fig. 21 the input condition corresponds to the square in Fig. 20 and the coupler is in the cross

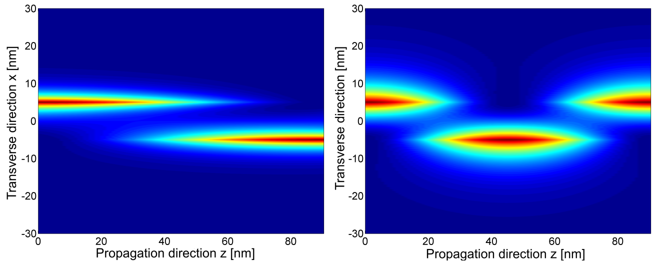

Fig. 21 Field evolution in a graphene plasmon directional coupler: left (right) refers to a chemical potential of $\mu_1 = 0.0908$ eV ($\mu_2 = 0.1367$ eV). Here $2s = 10nm$.

state; on the right panel the input condition corresponds to the circle in Fig. 20 and the coupler is in the bar state.

3.3 Graphene-Assisted Control of Coupling Between Optical Waveguides

In this subsection we demonstrate that, thanks to the ultrafast tunability of losses which are introduced by graphene layers deposited onto the structures, a careful design of silicon on insulator ridge waveguides can be used to explore the so-called passive parity-time (PT) symmetry breaking in directional couplers. A quantum system characterized by a Hamiltonian H is PT-symmetric if H commutes with the operator PT, where P is the parity operator and T is the temporal operator [83]. At an exceptional point, two or more eigenvalues are degenerate. We prove that the exceptional point of the coupler can be probed by varying the applied voltage, which may lead to very compact photonic structures for the control of coupling among waveguides, and for tailoring discrete diffraction in arrays [84].

In particular, in this section we present numerical results which demonstrate the huge potential of graphene as a means to control coupling between optical dielectric waveguides. The possibility of tuning losses in each waveguide by acting on a thin loss element permits to break the symmetry of the coupled waveguides, without introducing a strong perturbation in each single waveguide. Remarkably, we demonstrate that tunable losses induced by graphene and a careful design of ridge waveguides allows to probe passive PT-symmetry breaking in directional couplers [85, 86, 87]. Moreover, the exceptional point of the coupler can be dynamically controlled by varying the applied voltage. We will thus explore these properties to mould energy exchange between waveguides and to finely tune discrete diffraction in waveguide arrays. These results, together with the strong saturable absorption of graphene [75, 88], suggest also the possible use of this configuration in nonlinear devices with a strong pump beam used as a probe for all optical switching of weak input signals from the bar to cross state.

In order to prove our statement we first need to consider the behavior of silicon waveguides on a silica substrate in a wavelength range between 1350 and 1600 nm. The structure has been inspired by the modulator proposed in [89]. In particular, a layer of silicon with thickness equal to 50 nm is deposited onto the substrate. The 400 nm wide ridge waveguide is composed of lower and higher layers made of silicon (both with thickness 200 nm) which sandwich a central region including three alternating layers of alumina (thickness 7 nm) and two absorption layers composed of three graphene monolayers with thickness 0.34 nm. Graphene can be electrically controlled in order to tune doping (and then conductivity), as suggested in [89, 90, 91, 92, 93, 94, 95, 96]. The dielectric constants of silicon, silica and alumina were taken equal to 12.1, 2.1 and 3. Fig. 22(a) displays a schematic view of the structure.

The behavior of graphene in the optical regime has been numerically modeled by following the approach suggested in [81, 82], as already described in the previous subsection. Indeed, we assigned to each graphene monolayer with thickness Δ a volume conductivity equal to $\sigma_{g,v} = \sigma_{\Sigma}^{(1)}/\Delta$, where $\sigma_{\Sigma}^{(1)}$ is the conductivity of the 2D sheet (see Eq. 27 and Eqs. 28). It was demonstrated that, as a first approximation, few-layer graphene is characterized by the same band structure (and then by the same excellent electronic properties) of the monolayer. Moreover, if N is small enough the conductivity of N-layer graphene ($N = 3$ in our design) can be evaluated as N times conductivity of the single layer [91].

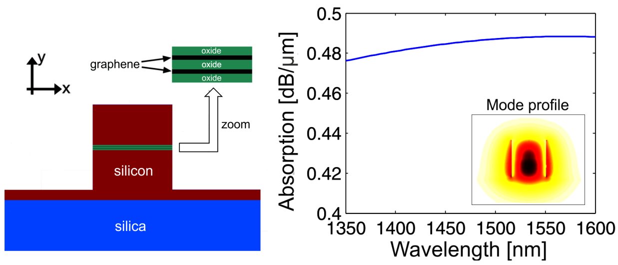

Fig. 22 (a) Schematic view of the waveguide structure, with a detail of the central region with graphene layers. (b) Losses of the single waveguide (in dB/μm) when graphene is in OFF state (null voltage), and x-component of the electric field of the TE-like mode (inset).

We then performed a modal analysis of the waveguide in Fig. 22(a) by resorting to finite-element simulations. We focused the attention on the TE-like mode which is depicted in the inset of Fig. 22(b), since the electric field is tangential with respect to graphene layers. In the same figure we report absorption of the TE-like mode when the graphene layers are in OFF state (null voltage). Of course, when graphene is in the ON state (a control voltage is applied), losses are close to zero. First, it is important to note that the real part of the effective index of the mode (not shown here) is barely affected by state of the graphene layers. Then, we emphasize that when graphene is in OFF state losses are quite large (0.48 dB/μm, which corresponds to 1100 cm^{-1}) and almost constant over the entire bandwidth: indeed, a

6 dB modulation contrast between ON and OFF states can be achieved with a 12.5 μm long waveguide. In the next paragraphs we will study the properties of coupled waveguides wherein the described structure is the basic building block.

Full-wave simulations of photonic devices including graphene layers are characterized by huge computational burden [98]. This effect is obviously emphasized when structures composed of multiple waveguides must be analyzed. Therefore conventional coupled-mode theory (CMT) [99, 100] has been reformulated to study the present structures. Using full wave simulations, we first numerically proved that neither the profile of TE-like modes, nor the propagation constant β of each isolated waveguide are affected by the status of graphene layers. Whereas switching between ON and OFF states has the effect of turning off and on losses in the single waveguide, which are modeled by the attenuation constant α. Notice that modal evolution reads as $\exp(i\beta z)\exp(-\alpha z)$.

Under these conditions, it is possible to verify that the system of governing equations for $A_{1,2}$, which are the modal field amplitudes in the first and second waveguide of a directional coupler composed of two identical graphene-based waveguides, can be approximated as

$$\frac{d}{dz}\begin{bmatrix} A_1 \\ A_2 \end{bmatrix} = i \begin{bmatrix} \beta + i\alpha_1 & C \\ C^* & \beta + i\alpha_2 \end{bmatrix} \begin{bmatrix} A_1 \\ A_2 \end{bmatrix}, \tag{30}$$

where $\alpha_{1,2}$ can be tuned between zero (ON state) and α_{max} (OFF state) by controlling the voltage applied to the graphene layers, and C is a complex coupling coefficient [86].

When $\alpha_1 = 0$ and $\alpha_2 = \alpha$, the eigenvalues of the matrix in Eq. 30 read as $\lambda_{1,2} = \beta + i(\alpha/2) \pm \sqrt{|C|^2 - (\alpha/2)^2}$. Therefore the so-called exceptional point (EP) for the onset of PT-symmetry breaking is located at the critical loss value $\alpha_c = 2C$. Indeed, when $\alpha < \alpha_c$ the two supermodes have different propagation constants and the same attenuation constant $\alpha/2$. Beyond the critical loss the supermodes coalesce: they are characterized by the same propagation constant β and by different loss coefficients. In particular, one supermode experiences increasing losses with increasing α, whereas the other supermode is characterized by the opposite trend [85, 86]. Whenever α is much larger than C, one supermode is characterized by losses which are close to the losses of a single waveguide, whereas the other supermode is nearly loss-free.

At this point we may examine the behavior of the directional coupler which is obtained by placing two identical graphene-based waveguides close to each other, separated by a 300 nm gap (see Fig. 23 on the left). We performed a modal analysis at 1530 nm focusing the attention on the supermodes which originate from the interaction between TE-like modes of the single waveguides, and we varied the state of the graphene layers. Numerical results in Fig. 23 illustrate in a qualitative way how the behavior of the structure can be controlled by exploiting the properties of graphene. In particular, when graphene layers in both waveguides are in the same state, the symmetry of the structure is preserved, and the two modes (not shown here) are even and odd. Viceversa, Fig. 23 shows that when symmetry is broken by switching to the ON-OFF state, the effect of losses on the modal properties is huge, and a trend toward decoupling between the waveguides is apparent.

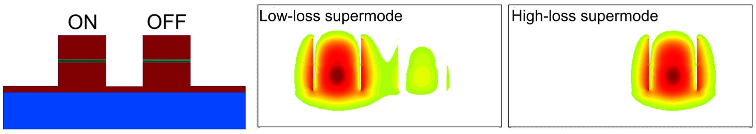

Fig. 23 Schematic view of the 300-nm-gap coupler (left), with the electric field of the low- (center) and high-loss mode (right) at 1530 nm. Graphene layers are in ON-OFF states.

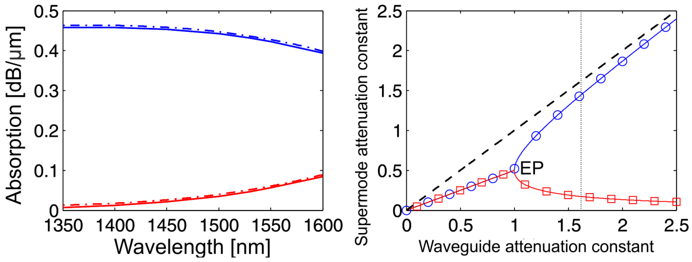

Fig. 24 (a) Losses of low- (red line) and high-loss mode (blue line) from mode solver (solid line) and CMT (dashed-dotted line). (b) Normalized attenuation constant of low- (red line with squares) and high-loss mode (blue line with circles) vs. normalized attenuation constant of the single waveguide at $\lambda = 1530$ nm. The vertical thin line indicates $\alpha = \alpha_{max}$.

The dispersive properties of the two modes have been characterized through full-wave and CMT simulations, and these quantitative results confirm the intuitive analysis we have reported above. Indeed, in Fig. 24(a) losses of the two supermodes are depicted when the graphene layers are in the ON-OFF state. In this case symmetry is broken: as a consequence, one mode is characterized by absorption which is close to zero, whereas the other mode experiences large losses, which are very close to those of a single lossy waveguide. It is worth noting that this effect tends to blur with increasing wavelength due to the dependence of coupling coefficient on frequency (C gets larger with increasing wavelength). A thorough treatment on phenomena arising from the wavelength dependence of the PT-symmetry condition is reported in [87]. The noticeable agreement in Fig. 24(a) between simulations performed by using a full-wave mode solver and the results evaluated by using CMT (in the latter case the imaginary part of $\lambda_{1,2}$ is reported) allows to confirm the accuracy of CMT.

These phenomena stem from the breaking of passive PT-symmetry in complex potentials. Indeed, in Fig. 24(b) we plot the attenuation constants of the two supermodes, evaluated by using CMT, as a function of the attenuation constant of the single waveguide α. Data are normalized with respect to twice the coupling coefficient, so that we have the exceptional point when the abscissa is equal to 1. The vertical dotted line indicates α_{max}, i.e. the value of α when our structure is in the

OFF state: it is straightforward to see that one may operate beyond the exceptional point, in agreement with the results of Fig. 24(a). It is worth to emphasize that graphene-based waveguides exhibit superior properties with respect to waveguides wherein losses are introduced by depositing metal layers [86]. Losses induced by sandwiching graphene layers inside silicon waveguides can be orders of magnitude larger (thousands of cm^{-1} with respect to tens of cm^{-1}), therefore it is possible to probe the exceptional point even in structures characterized by strong coupling. Last, but not least, it is important to note that graphene is electrically tunable, therefore losses in each single waveguide can be varied between zero (ON state) and a maximum value α_{max}, which is only determined by geometry (OFF state).

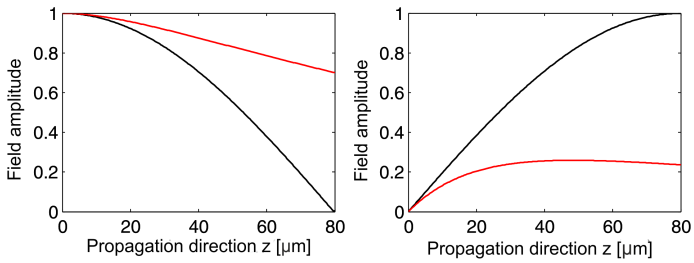

Fig. 25 Field amplitude in (a) first and (b) second waveguide of the coupler. Graphene layers are in ON-ON (black line), and ON-OFF (red line) states.

We envisage that switching of the state of one waveguide can be exploited to finely tune coupling between waveguides. In order to verify the effectiveness of this approach we applied CMT to our reference structure at the wavelength of 1530 nm, and we show the results in Fig. 25. When the coupler is in the ON-ON state losses are zero, and the predicted beat length $L_B = \pi/(\beta_{even} - \beta_{odd})$ is around 80 μm. Viceversa, when graphene layers are ON and OFF in the input and output channels, the two waveguides tend to decouple and the field intensity in the first waveguide is larger than in the second one. It is possible to justify this behavior by recalling that when we inject light into the waveguide in ON state the low-loss supermode is mainly excited.

These results have been validated by comparison with simulations of the 80 μm long coupler performed by using the commercial software CST Microwave Studio, which allows to solve Maxwell's equations in the time domain through the finite-integration technique. Indeed, the ratio between output and injected power evaluated by using CMT is -3 dB and -12 dB if the coupler is in the ON-OFF state and we consider as output port waveguides 1 and 2. CST simulations exhibit a good agreement, in fact the corresponding calculated values are about -5 dB and -13 dB, respectively.

The unique properties we have described in the previous paragraph open the way to novel possibilities for controlling discrete diffraction in waveguide arrays [99]-[104]. Let us take for example an array composed of eleven identical waveguides, with the same geometrical and optical parameters that we have used throughout

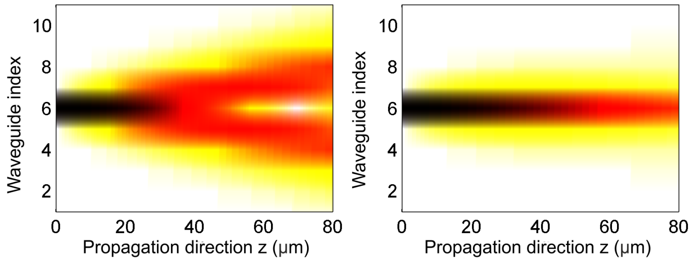

Fig. 26 Discrete diffraction along the array. (a) All the graphene layers are in ON state. (b) Only graphene layers inside the central waveguide are in ON state.

the Chapter, and the same spacing (300 nm) that we considered for the coupler. The structure was simulated by using CMT in order to reduce the computational burden. The input excitation covers only the central waveguide, and the propagation length was taken equal to the beat length of the coupler (80 μm). Moreover, we assumed that the state of the graphene layers in each waveguide can be controlled independently from each other.

In Fig. 26(a) we show the field inside the structure when all the graphene layers are in the ON state: the typical pattern of discrete diffraction is clearly visible, with two pronounced outermost wings [99, 100]. In Fig. 26(b) all the waveguides except for the central one are switched to the OFF state, and two phenomena can be clearly noticed. First, beam broadening is reduced with respect to the previous case, so that most of the optical energy remains concentrated into the central waveguide. Second, losses are smaller with respect to the case of a single lossy waveguide.

4 Conclusions

Optical switching will be a key enabling functionality in future transparent all–optical networks. In this chapter we have provided an overview of several guided wave optical switching devices, where the input–output path of optical signals is controlled by either optical or electrical signals, thus avoiding the need for OEO conversion for optical signal processing. We have first presented the basic principles of fiber optics switching devices, whose long interaction lengths permit to significantly reduce the operating power requirements. Next we have discussed nonlinear couplers based on integrated waveguides with strong field confinement, hence reduced device dimensions, thanks to photonic crystal structures or surface wave interactions in graphene layers.

Acknowledgements This work was funded by Fondazione Cariplo (grants no. 2011-0395 and no. 2013-0736), the Italian Ministry of University and Research (grant no. 2012BFNWZ2), and the US Army (grants no. W911NF-12-1-0590 and no. W911NF-13-1-0466).

References

1. Yariv, A.: Coupled-mode theory for guided-wave optics. IEEE Journ. Quantum Electron. **9**, 919–933 (1973)
2. Jensen, S. M.: The nonlinear coherent coupler. IEEE Journ. Quantum Electron. **18**, 1580–1583 (1982)
3. Maier, A. A.: Optical transistors and bistable devices utilizing nonlinear transmission of light in systems with undirectional coupled waves. Sov. J. Quantum Electron. **12**, 1490–1494 (1982)
4. Stegeman, G. I., Wright, E. M.: All-optical waveguide switching. Opt. Quant. Electron. **22**, 95–122 (1990)
5. Winful, H. G.: Self-induced polarization changes in birefringent optical fibers. Appl. Phys. Lett. **47**, 213–215 (1985)
6. Daino, B., Gregori, G., Wabnitz, S.: New all-optical devices based on third-order nonlinearity of birefringent fibers. Opt. Lett. **11**, 42–44 (1986)
7. Trillo, S., Wabnitz, S.: Nonlinear dynamics and instabilities of coupled waves and solitons in optical fibers. In: Someda, C. S., Stegeman, G. I. (eds.) Anisotropic and Nonlinear Optical Waveguides, pp. 185-236. Elsevier, Amsterdam (1992)
8. Daino, B., Gregori, G., Wabnitz, S.: Stability analysis of nonlinear coherent coupling. Journ. Appl. Phys. **58**, 4512–4514 (1985)
9. Winful, H. G.: Polarization instabilities in birefringent nonlinear media: application to fiber-optics devices. Opt. Lett. **11**, 33–35 (1986)
10. Wabnitz, S., Wright, E. M., Seaton, C. T., Stegeman, G. I.: Instabilities and all-optical phase-controlled switching in a nonlinear directional coherent coupler. Appl. Phys. Lett. **49**, 838–840 (1986)
11. Gusovskii, D. D., Dianov, E. M., Maier, A. A., Neustruev, V. B., Shklovskii, E. I., Shcherbakov, I. A.: Nonlinear light transfer in tunnel-coupled optical waveguides. Sov. J. Quantum Electron. **15**, 1523–1526 (1985)
12. Gusovskii, D. D., Dianov, E. M., Maier, A. A., Neustruev, V. B., Osiko, V. V., Prokhorov, A. M., Sitarskii, K. Yu., Shcherbakov, I. A.: Experimental observation of the self-switching of radiation in tunnel-coupled optical waveguides. Sov. J. Quantum Electron. **17**, 724–727 (1987)
13. Friberg, S. R., Silberberg, Y., Oliver, M. K., Andrejco, M. J., Saifi, M. A., Smith, P. W.: Ultrafast all-optical switching in a dual-core fiber nonlinear coupler. Appl. Phys. Lett. **51**, 1135–1137 (1987)
14. Weiner, A. M., Silberberg, Y., Friberg, S. R., Sfez, B. G., Smith, P.W.: Femtosecond all-optical switching in a dual-core fiber nonlinear coupler. Opt. Lett **13**, 904–906 (1988)
15. Weiner, A. M., Silberberg, Y., Fouckhardt, H., Leaird, D. E., Saifi, M. A., Andrejco, M. J., Smith, P. W.: Use of femtosecond square pulses to avoid pulse breakup in all-optical switching. IEEE J. Quantum Electron. **25**, 2648–2655 (1989)
16. Trillo, S., Wabnitz, S., Stolen, R. H., Assanto, G., Seaton, C. T., Stegeman, G. I.: Experimental observation of polarization instability in a birefringent optical fiber. Appl. Phys. Lett. **49**, 1224–1226 (1986)
17. Trillo, S., Wabnitz, S., Banyai, W. C., Finlayson, N., Seaton, C. T., Stegeman, G. I., Stolen, R. H.: Picosecond nonlinear polarization switching with a fiber filter. Appl. Phys. Lett. **53**, 837–839 (1988)
18. Trillo, S., Wabnitz, S., Banyai, W. C., Finlayson, N., Seaton, C. T., Stegeman, G. I., Stolen, R. H.: Observation of ultrafast nonlinear polarization switching induced by polarization instability in a birefringent fiber rocking filter. IEEE J. Quantum Electron. **25**, 104–112 (1989)
19. Ferro, P., Haelterman, M., Trillo, S., Wabnitz, S., Daino, B.: Polarization switching in spun birefringent fiber. Appl. Phys. Lett. **59**, 2082–2084 (1991)
20. Ferro, P., Haelterman, M., Trillo, S., Wabnitz, S., Daino, B.: All-optical polarization switch with a long low-birefringence fiber. Electron. Lett. **27**, 1407–1408 (1991)

21. Ferro, P., Trillo, S., Wabnitz, S.: All-optical polarization differential amplification with a birefringent fiber. Electron. Lett. **30**, 1616–1617 (1994)
22. Ferro, P., Trillo, S., Wabnitz, S.: Phase control of a nonlinear coherent coupler: the multi-beatlength twisted birefringent fiber. Appl. Phys. Lett. **64**, 2872–2874 (1994)
23. Ferro, P., Trillo, S., Wabnitz, S.: Demonstration of nonlinear nonreciprocity and logic operations with a twisted birefringent optical fiber. Opt. Lett. **19**, 263–265 (1994)
24. Doran, N. J., Wood, D.: Soliton processing element for all-optical switching and logic. J. Opt. Soc. Am. B **4**, 1843–1846 (1987)
25. Imoto, N., Watkins, S., Sasaki, Y.: A nonlinear optical-fiber interferometer for nondemolitional measurement of photon number. Opt. Commun. **61**, 159–163 (1987)
26. Nayar, B. K., Finlayson, N., Doran, N. J., Davey, S. T., Williams, W. L., Arkwright, J. W.: All-optical switching in a 200-m twin-core fiber nonlinear Mach-Zehnder interferometer. Opt. Lett. **16**, 408–410 (1991)
27. Asobe, M.: Effects of group-velocity dispersion in all-optical switching devices using highly nonlinear optical waveguides. J. Opt. Soc. Am. B **12**, 1287–1299 (1995)
28. Otsuka, K.: Nonlinear antiresonant ring interferometer. Opt. Lett. **8**, 471–473 (1983)
29. Mortimore, D. B.: Fiber loop reflectors, J. Lightwave Technol. **6**, 1217–1224 (1988)
30. Doran, N. J., Wood, D.: Nonlinear optical loop mirror. Opt. Lett. **13**, 56–58 (1988)
31. Doran, N. J., Forrester, D. S., Nayar, B. K.: Experimental investigation of all-optical switching in a fibre loop mirror device. Electron. Lett. **25**, 267–268 (1989)
32. Blow, K. J., Doran, N. J., Nayar, B. K.: Experimental demonstration of optical soliton switching in an all-fiber nonlinear Sagnac interferometer Opt. Lett. **14**, 754–756 (1989)
33. Islam, M. N., Sunderman, E. R., Stolen, R. H., Pleibel, W., Simpson, J. R.: Soliton switching in a fiber nonlinear loop mirror. Opt. Lett. **14**, 811–813 (1989)
34. Farries, M. C., Payne, D. N.: Optical fiber switch employing a Sagnac interferometer. Appl. Phys. Lett. **55**, 25–26 (1989)
35. Blow, K. J., Doran, N. J., Nayar, B. K., Nelson, B. P.: Pulse shaping, compression, and pedestal suppression employing a nonlinear-optical loop mirror. Opt. Lett. **15**, 248–250 (1990)
36. Jinno, M., Matsumoto, T.: Ultrafast, low power, and highly stable all-optical switching in an all polarization maintaining fiber Sagnac interferometer. IEEE Photon. Technol. Lett. **2**, 349–351 (1990)
37. Jinno, M., Matsumoto, T.: Ultrafast all-optical logic operations in a nonlinear Sagnac interferometer with two control beams Opt. Lett., **16**, 220–222 (1991)
38. Stokes, L. F., Chodorow, M., Shaw, H. J.: All-single-mode fiber resonator. Opt. Lett. **7**, 288–290 (1982)
39. Nakatsuka, H., Asaka, S., Itoh, H., Ikeda, K., Matsuoka, M.: Observation of bifurcation to chaos in an all-optical bistable system. Phys. Rev. Lett. **50**, 109–112 (1983)
40. Crosignani, B., Daino, B., Di Porto, P., Wabnitz, S.: Optical multistability in a fiber-optic passive-loop resonator. Opt. Commun. **59**, 309–312 (1986)
41. Haelterman, M., Trillo, S., Wabnitz, S.: Dissipative modulation instability in a nonlinear dispersive ring cavity. Opt. Commun. **91**, 401–407 (1992)
42. Coen, S., Haelterman, M., Emplit, P., Delage, L., Simohamed, L. M., Reynaud, F.: Experimental investigation of the dynamics of a stabilized nonlinear fiber ring resonator. J. Opt. Soc. Am. B **15**, 2283–2293 (1998)
43. Trillo, S., Wabnitz, S., Wright, E. M., Stegeman, G. I.: Soliton switching in fiber nonlinear directional couplers. Opt. Lett. **13** 672–674 (1988)
44. Trillo, S., Wabnitz, S.: Weak-pulse-activated soliton switching in nonlinear couplers. Opt. Lett. **16**, 1–3 (1991)
45. Romagnoli, M., Trillo, S., Wabnitz, S.: Soliton switching in nonlinear couplers. Opt. Quant. Electron. **24**, S1237–S1267 (1992)
46. Joannopoulos, J. D., Meade, R. D., Winn, J. N.: Photonic Crystals: Molding the Flow of Light. Princeton University Press, Princeton (1995)
47. Joannopoulos, J. D., Villeneuve, P. R., Fan, S.: Photonic crystals: Putting a new twist on light. Nature **386**, 143–149 (1997)

48. Soljacic, M., Ibanescu, M., Johnson, S. G., Fink, Y., Joannopoulos, J. D.: Optimal bistable switching in nonlinear photonic crystals. Phys. Rev. E **66**, 055601 (2002)
49. Mingaleev, S. F., Kivshar, Y. S.: Nonlinear transmission and light localization in photonic-crystal waveguides. J. Opt. Soc. Am. B **19**, 2241–2249 (2002)
50. Soljacic, M., Luo, C., Joannopoulos, J. D., Fan, S.: Nonlinear photonic crystal microdevices for optical integration. Opt. Lett. **28**, 637–639 (2003)
51. Boscolo, S., Midrio, M., Someda, C. G.: Coupling and decoupling of electromagnetic waves in parallel 2-D photonic crystal waveguides. IEEE Journ. Quantum Electron. **38**, 47–53 (2002)
52. Martinez, A., Cuesta, F., Marti, J.: Ultrashort 2-D photonic crystal directional couplers. IEEE Photon. Technol. Lett. **15**, 694–696 (2003)
53. Thorhauge, M., Frandsen, L. H., Borel, P. I.: Efficient photonic crystal directional couplers. Opt. Lett. **28**, 1525–1527 (2003)
54. Taflove, A., Hagness, S. C.: Computational Electrodynamics: the finite-difference time-domain method. Artech House, Norwood (2000)
55. Joseph, R. M., Taflove, A.: FDTD Maxwell's equations models for nonlinear electrodynamics and optics. IEEE Trans. Antennas Propagat. **45**, 364–374 (1997)
56. Aitchison, J. S., Hutchings, D. C., Kang, J. U., Stegeman, G. I., Villeneuve, A.: The nonlinear optical properties of AlGaAs at the half band gap. IEEE Journ. Quantum Electron. **33**, 341–348 (1997)
57. Johnson, S. G., Villeneuve, P. R., Fan, S., Joannopoulos, J. D.: Linear waveguides in photonic-crystal slabs. Phys. Rev. B **62**, 8212–8222 (2000)
58. Johnson, S. G., Joannopoulos, J. D.: Block-iterative frequency-domain methods for Maxwell's equations in a planewave basis. Opt. Express **8**, 173–190 (2001)
59. Happ, T. D., Kamp, M., Forchel, A.: Photonic crystal tapers for ultracompact mode conversion. Opt. Lett. **26**, 1102–1104 (2001)
60. Bienstman, P., Assefa, S., Johnson, S. G., Joannopoulos, J. D., Petrich, G. S., Kolodziejski, L. A.: Taper structures for coupling into photonic crystal slab waveguides. J. Opt. Soc. Am. B **20**, 1817–1821 (2003)
61. Reynolds, A. L., Peschel, U., Lederer, F., Roberts, P. J., Krauss, T. F., de Maagt, P. J. I.: Coupled defects in photonic crystals. IEEE Trans. Microwave Theory Tech. **49**, 1860–1867 (2001)
62. Peschel, U., Reynolds, A. L., Arredondo, B., Lederer, F., Roberts, P. J., Krauss, T. F., de Maagt, P. J. I.: Transmission and reflection analysis of functional coupled cavity components. IEEE Journ. Quantum Electron. **38**, 830–836 (2002)
63. Christodoulides, D. N., Efremidis, N. K.: Discrete temporal solitons along a chain of nonlinear coupled microcavities embedded in photonic crystals. Opt. Lett. **27**, 568–570 (2002)
64. Al-hemyari, K., Villeneuve, A., Kang, J. U., Aitchison, J. S., Ironside, C. N., Stegeman, G. I.: Ultrafast all-optical switching in GaAlAs directional couplers at 1.55 μm without multiphoton absorption. Appl. Phys. Lett. **63**, 3562–3564 (1993)
65. Aitchison, J. S., Villeneuve, A., Stegeman, G. I.: All-optical switching in two cascaded nonlinear directional couplers. Opt. Lett. **20**, 698–700 (1995)
66. Auditore, A., De Angelis, C., Locatelli, A., Aceves, A. B.: Tuning of surface plasmon polaritons beat length in graphene directional couplers. Opt. Lett. **38**, 4228–4231 (2013).
67. Auditore, A., De Angelis, C., Locatelli, A., Boscolo, S., Midrio, M., Romagnoli, M., Capobianco, A.-D., Nalesso, G.: Graphene sustained nonlinear modes in dielectric waveguides. Opt. Lett. **38**, 631–633 (2013)
68. Smirnova, D. A., Gorbach, A. V., Iorsh, I. V., Shadrivov, I. V., Kivshar, Y. S.: Nonlinear switching with a graphene coupler. Phys. Rev. B **88**, 045433 (2013)
69. Buslaev, P. I., Iorsh, I. V., Shadrivov, I. V., Belov, P. A., Kivshar, Y. S.: Plasmons in waveguide structures formed by two graphene layers. JETP Lett. **97**, 535–539 (2013)
70. Locatelli, A., Capobianco, A.-D., Nalesso, G., Boscolo, S., Midrio, M., De Angelis, C.: Graphene based electro-optical control of the beat length of dielectric couplers. Opt. Commun. **318**, 175–179 (2014)

71. Bludov, Yu. V., Smirnova, D. A., Kivshar, Yu. S., Peres, N. M. R., Vasilevskiy, M. I.: Nonlinear TE-polarized surface polaritons on graphene. Phys. Rev. B **89**, 035406 (2014)
72. Mikhailov, S. A., Ziegler, K.: New electromagnetic mode in graphene. Phys. Rev. Lett. **99**, 016803 (2007)
73. Mikhailov, S. A., Ziegler, K.: Nonlinear electromagnetic response of graphene: frequency multiplication and the self-consistent-field effects. J. Phys.: Condens. Matter **20**, 1–10 (2008)
74. Jablan, M., Buljan, H., Soljacic, M.: Plasmonics in graphene at infra-red frequencies. Phys. Rev. B **80**, 245435 (2009)
75. Zhang, H., Virally, S., Bao, Q., Ping, L. K., Massar, S., Godbout, N., Kockaert, P.: Z-scan measurement of the nonlinear refractive index of graphene. Opt. Lett. **37**, 1856–1858 (2012)
76. Gorbach, A. V.: Nonlinear graphene plasmonics: amplitude equation for surface plasmons. Phys. Rev. A **87**, 013830 (2013)
77. Ju, L., Geng, B., Horng, J., Girit, C., Martin, M., Hao, Z., Bechtel, H. A., Liang, X., Zettl, A., Shen, Y. R., Wang, F.: Nat. Nanotechnol. **6**, 630 (2011)
78. Chen, J., Badioli, M., Alonso-Gonzalez, P., Thongrattanasiri, S., Huth, F., Osmond, J., Spasenovic, M., Centeno, A., Pesquera, A., Godignon, P., Zurutuza Elorza, A., Camara, N., Javier Garcia De Abajo, F., Hillenbrand, R., Koppens, F. H. L.: Optical nano-imaging of gate-tunable graphene plasmons, Nature **486**, 77–81 (2012)
79. Fei, Z., Rodin, A. S., Andreev, G. O., Bao, W., McLeod, A. S., Wagner, M., Zhang, L. M., Zhao, Z., Dominguez, G., Thiemens, M., Fogler, M. M., Castro-Neto, A. H., Lau, C. N., Keilmann, F., Basov, D. N.: Gate-tuning of graphene plasmons revealed by infrared nano-imaging. Nature **487**, 82–85 (2012)
80. Wang, B., Zhang, X., Yuan, X., Teng, J.: Optical coupling of surface plasmons between graphene sheets. Appl. Phys. Lett. **100**, 131111 (2012)
81. Vakil, A., Engheta, N.: Transformation optics using graphene. Science **332**, 1291–1294 (2011)
82. Stauber, T., Peres, N. M. R., Geim, A. K.: Optical conductivity of graphene in the visible region of the spectrum. Phys. Rev. B **78**, 085432 (2008)
83. Bender, C. M., Boettcher, S.: Real spectra in non-Hermitian Hamiltonians having PT symmetry. Phys. Rev. Lett. **80**, 5243–5246 (1998)
84. Locatelli, A., Capobianco, A.-D., Midrio, M., Boscolo, S., De Angelis, C.: Graphene-assisted control of coupling between optical waveguides. Opt. Express **20**, 28479 (2012)
85. Klaiman, S., Gunther, U., Moiseyev, N.: Visualization of branch points in PT-symmetric waveguides. Phys. Rev. Lett. **101**, 080402 (2008)
86. Guo, A., Salamo, G. J., Duchesne, D., Morandotti, R., Volatier-Ravat, M., Aimez, V., Siviloglou, G. A., Christodoulides, D. N.: Observation of PT-symmetry breaking in complex optical potentials. Phys. Rev. Lett. **103**, 093902 (2009)
87. Yu, S., Piao, G. X., Mason, D. R., In, S., Park, N.: Spatiospectral separation of exceptional points in PT-symmetric optical potentials. Phys. Rev. A **86**, 031802 (2012)
88. Yang, H., Feng, X., Wang, Q., Huang, H., Chen, W., Wee, A. T. S., Ji, W.: Giant two-photon absorption in bilayer graphene," Nano Lett. **11**, 2622–2627 (2011)
89. Kim, K., Choi, J. Y., Kim T., Cho, S. H., Chung, H. J.: A role for graphene in silicon-based semiconductor devices. Nature **479**, 338–344 (2011)
90. Bonaccorso, F., Sun, Z., Hasan, T., Ferrari, A. C.: Graphene photonics and optoelectronics. Nat. Photon. **4**, 611–622 (2010)
91. Liu, M., Yin, X., Ulin-Avila, E., Geng, B., Zentgraf, T., Ju, L., Wang, F., Zhang, X.: A graphene-based broadband optical modulator. Nature **474**, 64–67 (2011)
92. Liu, M., Yin, X., Zhang, X.: Double-layer graphene optical modulator. Nano Lett. **12**, 1482–1485 (2012)
93. Midrio, M., Boscolo, S., Moresco, M., Romagnoli, M., De Angelis, C., Locatelli, A., Capobianco, A.-D.: Graphene-assisted critically-coupled optical ring modulator. Opt. Express **20**, 23144–23155 (2012)
94. Bao, Q., Zhang, H., Wang, B., Ni, Z., Lim, C., Wang, Y., Tang, D. Y., Loh, K. P.: Broadband graphene polarizer. Nat. Photon. **5**, 411–415 (2011)

95. Kim, J. T., Choi, C. G.: Graphene-based polymer waveguide polarizer. Opt. Express **20**, 3556–3562 (2012)
96. Li, Z. Q., Henriksen, E. A., Jiang, Z., Hao, Z., Martin, M. C., Kim, P., Stormer, H. L., Basov, D. N.: Dirac charge dynamics in graphene by infrared spectroscopy. Nat. Phys. **4**, 532–535 (2008)
97. Hanson, G. W.: Dyadic Green's functions for an anisotropic, non-local model of biased graphene. IEEE Trans. Antennas Propagat. **56**, 747–757 (2008)
98. Capobianco, A.-D., Locatelli, A., De Angelis, C., Midrio, M., Boscolo, S.: Finite-difference beam propagation method for graphene-based devices. IEEE Photon. Technol. Lett. **26**, 1007–1010 (2014)
99. Christodoulides, D. N., Joseph, R. I.: Discrete self-focusing in nonlinear arrays of coupled waveguides. Opt. Lett. **13**, 794–796 (1988)
100. Pertsch, T., Zentgraf, T., Peschel, U., Brauer, A., Lederer, F.: Anomalous refraction and diffraction in discrete optical systems. Phys. Rev. Lett. **88**, 093901 (2002)
101. Locatelli, A., Conforti, M., Modotto, D., De Angelis, C.: Diffraction engineering in arrays of photonic crystal waveguides. Opt. Lett. **30**, 2894–2896 (2005)
102. Locatelli, A., Conforti, M., Modotto, D., De Angelis, C.: Discrete negative refraction in photonic crystal waveguide arrays. Opt. Lett. **31**, 1343–1345 (2006)
103. Guasoni, M., Locatelli, A., De Angelis, C.: Peculiar properties of photonic crystal binary waveguide arrays. J. Opt. Soc. Am. B **25**, 1515–1522 (2008)
104. Conforti, M., Guasoni, M., De Angelis, C.: Subwavelength diffraction management. Opt. Lett. **33**, 2662–2664 (2008)